# Significance of the Compliance of the Joints on the Dynamic Slip Resistance of a Bioinspired Hoof

Sara-Adela Abad, Nicolas Herzig, Seyedmohammadhadi M. Hadi Sadati, and Thrishantha Nanayakkara

***Abstract*—Robust mechanisms for slip resistance are an open challenge in legged locomotion. Animals such as goats show impressive ability to resist slippage on cliffs. It is not fully known what attributes in their body determine this ability. Studying the slip resistance dynamics of the goat may offer insight toward the biologically inspired design of robotic hooves. This article tests how the embodiment of the hoof contributes to solving the problem of slip resistance. We ran numerical simulations and experiments using a passive robotic goat hoof for different compliance levels of its three joints. We established that compliant yaw and pitch and stiff roll can increase the energy required to slide the hoof by $\approx 20\%$ compared to the baseline (stiff hoof). Compliant roll and pitch allow the robotic hoof to adapt to the irregularities of the terrain. This produces an antilock braking system-like behavior of the robotic hoof for slip resistance. Therefore, the pastern and coffin joints have a substantial effect on the slip resistance of the robotic hoof, while the fetlock joint has the lowest contribution. These shed insights into how robotic hooves can be used to autonomously improve slip resistance.**

***Index Terms*—Biologically inspired robots, compliant joint/mechanism, legged robots, slip resistance.**

Manuscript received November 27, 2018; accepted June 26, 2019. Date of publication August 20, 2019; date of current version December 3, 2019. This work was supported in part by the Ecuadorian Government through Secretaria de Educacion Superior, Ciencia, Tecnologia e Innovacion code AR2Q-5232, and in part by the U.K. Engineering and Physical Sciences Research Council under Grant EP/I028765/1, Grant EP/I028773/1, and Grant EP/N03211X/1. This article was recommended for publication by Associate Editor P.-C. Lin and Editor I.-M. Chen upon evaluation of the reviewers' comments. *(Corresponding author: Sara-Adela Abad.)*

S.-A. Abad is with the Dyson School of Design Engineering, Imperial College London, SW7 2DB London, U.K., and also with the Institute for Applied Sustainability Research, Quito 170503, Ecuador (e-mail: s.abad-guaman17@imperial.ac.uk).

N. Herzig is with the Dyson School of Design Engineering, Imperial College London, SW7 2DB London, U.K. (e-mail: n.herzig@imperial.ac.uk).

S. M. H. Sadati is with the Department of Engineering Mathematics, University of Bristol, BS8 1TH Bristol, U.K. (e-mail: s.m.hadi.sadati@bristol.ac.uk).

T. Nanayakkara is with the Dyson School of Design Engineering, Imperial College London, SW7 2DB London, U.K. (e-mail: t.nanayakkara@imperial.ac.uk).

This article has supplementary downloadable material available at http://ieeexplore.ieee.org, provided by the authors. The material consists of a video illustrating the movement of the hoof of an Ecuadorian mountain goat walking downhill. It shows how the goat opens the claws for adapting the position of the claws to the terrain and increasing the probability of finding firm terrain. Then, it can be noticed that the goat open the claws in the deformable terrain to hold some rocks between the claws (in the interdigital cleft) to increase the braking force. The video shows the setup, which comprises the length and direction of the sliding path of the hoof, the force sensor, the Vicon system for tracking the position of the components of the hoof, the relatively smooth hard terrain, and the *XY* stage (actuator) that moves the hoof. The video also shows one trial of the experiment; it shows the lateral view in the top left corner, the tracking of the markers using the Vicon system in the top right corner, and the profile of the force applied in the sliding direction of the hoof at the coupling point between the rigid leg and the *XY* stage. At the end, the experiments for a relatively stiff combination and a compliant combination are shown. For the former, the tip of the claw exhibits a slight uneven up and down movement, while for the compliant combination, this movement is smooth. Contact Sara-Adela Abad (e-mail: s.abad-guaman17@imperial.ac.uk) for further questions about this work.

Color versions of one or more of the figures in this article are available online at http://ieeexplore.ieee.org.

Digital Object Identifier 10.1109/TRO.2019.2930864

## I. Introduction

In RECENT years, there has been a growing interest to understand how dynamics of a physical agent can be used to simplify the computations required to survive in a real environment [1]. For instance, the robotic cheetah [2], RHex [3], and SpinybotII [4] use relatively simple controllers to achieve complex dynamic maneuvers like running at 4.5 m/s in the case of the robotic cheetah [5], walking over unstructured terrain with a simple control in Rhex [3], and climbing over vertical surfaces in SpinybotII [4]. Though two robots cannot be compared easily, the IMPASS robot [6], which has individually actuated spokes of the rimless wheels called whegs, has higher control complexity and power consumption than RHex, which has a better physical solution at the foot level. However, the stability of robots in inclined terrain conditions is still limited due to the computations needed.

Recently, investigators are examining the Capra hircus [7]–[10] due to their impressive climbing capabilities. Using *in vivo* experiments, they studied the behavior of the muscles and tendons of the hindlimb for inclined, declined, and level running. They conclude that the ankle, knee, and hip generate energy for inclined running. For declined running, the energy is mainly absorbed in the ankle and knee. Moreover, the joint between the hoof and the ankle (fetlock joint) is mainly absorbing energy during decline, level, and inclined running [8]. This energy-absorbing behavior may have an important role in the remarkable climbing capabilities. However, even though McGeer and Palmer showed that the feet morphology affects the stability of legged robots [11], little research has been done about the hoof of the goat illustrated in Fig. 1.

In the past few years, Zhang *et al.* [12], [13] have studied the hoof of large ruminants using only numerical analysis of a generic hoof. Since they are trying to replicate most of the features of the hoof, their proposed models are complex.

On the other hand, using a static model and preliminary experimental results for eight combinations of compliance levels of the three joints of the hoof (fetlock, pastern, and coffin joints illustrated in Fig. 2), Abad *et al.* [14] showed that the work required to slide a robotic hoof over a wooden brick can be three

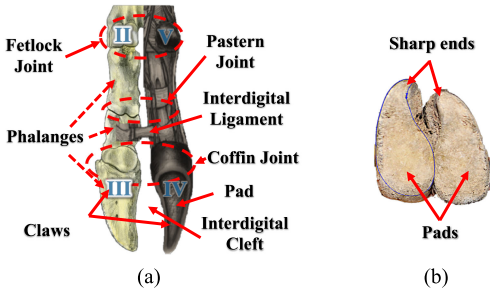


Fig. 1. Biological goat hoof. (a) Bones, ligaments, and tissue distribution of the biological hoof used for the design (adapted from [15, Plate 4.7] and [16, Fig. 2.10]). (b) Profile of the goat claw, which was used to design the robotic hoof in this article.

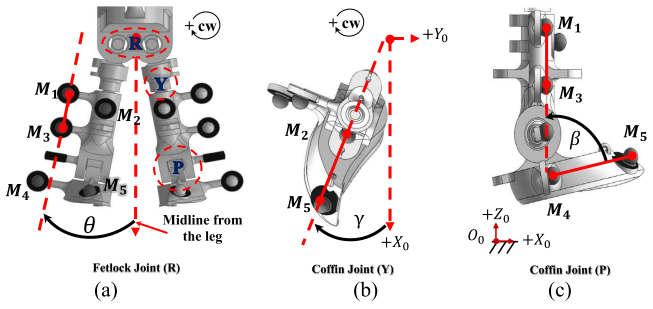


Fig. 2. DOF of the robotic hoof. For simplicity, they are defined as roll (R), yaw (Y), and pitch (P). (a) R is measured using the angle of the fetlock joint $\theta$. (b) Y is defined by the angle of the pastern joint $\gamma$. (c) P is quantified by the angle of the coffin joint $\beta$.

times higher than that of a rounded foot (common design), the work depends not only on the shape of the foot, but also on the compliance of its joints, and the role of the joints changes with the roughness of the environment.

For simplicity, in this article, we define the movement of the fetlock, coffin, and pastern joints (shown in Fig. 2) as the roll, yaw, and pitch of the robotic hoof, respectively. The movement of the joints is denoted using the angles $\theta$, $\gamma$, and $\beta$, respectively. Each joint imposes a mechanical impedance on the movements of the robotic hoof.

The results presented in [14] provide an insight into the dynamic behavior of the hoof. It shows that when the hoof slips against a surface, the hoof presents a stick and slip behavior. This behavior may rise vibrations that propagate along the mechanical circuit of the hoof (bone-ligament structure in the above joints) potentially generating punctuated interaction forces like in the antilock braking system (ABS) of automobile brakes.

In the ABS, there are punctuated braking forces in order to apply and release the brake pressure in a tire to keep tire's adhesion coefficient near its maximum; this process limits the slip between the tire and the road surface [17]–[19].

It is worth investigating the question as to whether passive interaction dynamics of the hoof contributes to improving slip resistance on a given roughness of the contact surface. The contribution of these passive interactions can be analyzed in terms of external energy needed to slide the hoof. Therefore, when the punctuated forces cause the stick and slip behavior observed in [14], the system also takes into account the friction force dissipated energy and the variation on the potential energy stored in the spring-like mechanisms, where the higher the external energy value, the higher the slip resistance. As a consequence, the LuGre friction model is used to capture the dynamic stick-slip behavior of the hoof.

A deeper understanding of these passive interaction dynamics will provide new insights to design foot mechanisms for legged robots. Consequently, using a dynamic model and experimental results, the aims of this article are: 1) to determine the most significant compliance combinations across all joints to improve the slip resistance of the hoof and 2) to understand the individual contribution of the joints on the slip resistance of the hoof.

This article corroborates and extends our previous study [14] by using a model of the hoof's dynamic behavior, testing 64 combinations of compliance levels of the three joints, and having a closer look at the contribution of each joint on the slip resistance of the hoof. We found that since the compliance of each joint in the hoof is a critical vector of morphological parameters determining the slip resistance of the hoof, having a compliant pitch and yaw and stiff roll can increase the energy required to slide the hoof by $\approx 20\%$ compared to the energy of the stiff combination (baseline), and that the coffin (pitch) and pastern (yaw) joints have a significant contribution in the slip resistance, while that of the fetlock joint (roll) is minimal. This is because having complaint yaw and pitch allows the hoof to adapt to the irregularities of the terrain. Because of this, an oscillatory behavior at the pitch emerges that produces an ABS-like behavior at the hoof for reducing the speed. This sheds new insights on further simplification of the robotic hoof, while improving their slip resistance capabilities.

The rest of this article is organized as follows. Section II describes the biology of the goats' hoof, gives the analytic model used to describe the dynamic behavior of the hoof, and presents the design of the robotic hoof. Section III explains the utilized methodology for the numerical analysis and the experiments. Section IV presents the analytic and experimental results. Then, Section V discusses the results, and Section VI concludes this article.

## II. Analytical Model and Design of the Biologically Inspired Foot

This article aims to understand the effect of the compliance level of the joints in the dynamics of the embodiment and the contribution of each joint on improving the slip resistance. A robotic hoof was chosen because hoofed animals show outstanding capabilities for walking over muddy or rocky terrains.

The main features of their feet structure are their hoofs, pads, and bone structure that suit their ecological niches. In fact, pigs live in muddy terrains. They have two declaws and two straight claws [analogous to the claws III and IV, and II and V, presented in Fig. 1(a)]. Since all four are fully developed, the declaws improve the stability of the pigs when they are sunk in mud [20]. On the other hand, camels avoid sinking in the sand by increasing

the contact area between the foot and the ground, which reduces the pressure on the sand. This is possible due to their two-toed feet, the lack of a proximal interdigital ligament, and the broad pads under the toes that flatten due to the weight [21].

Among all the ungulates, goats have been chosen as biological inspiration because they are well known for walking over mountains, including climbing trees and dams. Moreover, earlier, we have shown evidence that compliant hoof joints improve slip resistance [14]. Therefore, before presenting the detailed analysis and experiments to study the physical features of the hoof, it is necessary to understand the anatomy of the biological hoof.

### A. Biomechanical Description of the Goats' Hoof

Goats as well as other cloven-hoofed animals such as bovines, sheep, and deer present digits with their distal end covered with hard keratin, and the structure of the hoof comprised of three joints (fetlock, pastern, and coffin joint) is also similar [13]. The digits can differ in dimension, the shape of the claws, and declaws. Since there is limited information regarding the goat hoof, its biomechanical description has been complemented using information from blue sheep [22] and bovines [23], [24].

The main features of the hoof presented in Fig. 1 are the following:

1) The claws are closed together while they are in the air, but they spread apart when touching the ground to transfer the weight of the body to the hoof [22].
2) At the bottom of the toes, goats have a rough pliant textured pad that is slightly projected over the nail; it increases the contact area with smooth surfaces and absorbs shocks [see Fig. 1(b)].
3) The frontal tip of the toes facilitates digging into the soil for walking uphill.
4) The V-shaped disposition of the claws and the interdigital cleft help to stick in the soil to generate braking forces.
5) Flexion/extension (denoted as pitch) is produced by tendons actuated by muscles.
6) Flexion/extension is the main and common motion to all the three hoof joints, but the coffin joint is the one with the highest effect on the pitch.
7) The natural dynamics of the hoof interacting with the environment passively produce claw's abduction/adduction (denoted as roll) and rotation (denoted as yaw).
8) The roll of the claw is imposed by the fetlock or metacarpophalageal joint [23], [24], and the compliance of this joint is set by the distal and proximal interdigital ligaments. This increases the likelihood of standing over a firm terrain. Additionally, the lateral movement of the toes produces slip dissipation orthogonal to the walking direction that generates a natural stabilizing effect when the goat walks downhill as observed in the Oreamnos americanus [25]. In this article, it is assumed that the latter observation is also valid for the Capra hircus.
9) Claw's rotation is mainly imposed by the coffin or distal interphalangeal joint. Therefore, the compound pitch and yaw rotation of the coffin joint produces a screw-like rotation of the claw [23].

Having defined the biomechanical properties of the hoof, the following subsections present the models utilized for the analysis of the hoof's behavior.

### B. System's Dynamics

Based on the biomechanics of the goat hoof described in the previous section and the existing research in passive dynamics [1], [3], [11], we believe that not only the active flexion/extension plays an important role in the slip resistance, yaw and roll together with the natural dynamics of the hoof may contribute as well. Consequently, the features of the biological hoof have been simplified by only assigning one degree of freedom (DOF) per joint in the robotic hoof as follows.

1) The coffin joint defines the pitch movement (flexion/extension) to improve the adaptability of the claw to the irregularities of the terrain.
2) The fetlock joint defines the roll movement (abduction/adduction of the claw).
3) The pastern joint defines the yaw (rotation).

Furthermore, for accomplishing a passive robotic hoof, pitch compliance was set using antagonistic springs. The advantage of this simplification is that the design of the robotic hoof can be passive, simpler, and not redundant (this means that the common flexion/extension motion in the joints of the biological hoof was given to only one joint in the robotic hoof).

Similarly, for simplification, the numerical analysis of the hoof is based on the following assumptions.

1) The effects of the other parts of the body dynamics are modeled as an external force, $f_s$, that slides the hoof; this force resembles the component of the weight that is parallel to the sliding plane that is pushing down the goat.
2) $f_s$ induces the translation of $O_1$ at constant speed ($v_1 = 0.01$ m/s in this case) along $\mathbf{x}'_0$ (see Fig. 3).
3) The hoof is symmetric with respect to the medial plane between the claws; therefore, the left claw was chosen for the analytic study.
4) The joint at $O_2$ [see Fig. 3(a)] can be modeled as a revolute joint with damping $c_\phi$, stiffness $k_\phi$, and free position angle of spring equal to $18^\circ$.
5) Due to the sole, a claw is modeled as a segment of a circle with radius $R$, which is always aligned with the plane $(\ 0_6, \mathbf{x_6}, \mathbf{y_6}\ )$, as shown in Fig. 4.
6) For simplicity of analysis, we consider a single contact point denoted $I$ between the claw and the ground. Following the previous assumption: $I \in (\ 0_6, \mathbf{x_6}, \mathbf{y_6}\ )$.
7) The claws are always in contact with the ground at $I$; this point can move along the simplified circular contact surface.
8) The prismatic joint between links 2 and 3 has stiffness $k_{23}$ and damping $c_{23}$; the purpose of this joint is to passively affect the normal force during the experiment.
9) The external mechanism that generates $f_s$ can be modeled as an actuated prismatic ideal joint.
10) The vertical distance between $O_2$ and $I$ remains constant. Thus, $\mathbf{IO_2}.\mathbf{z_0} = H$.

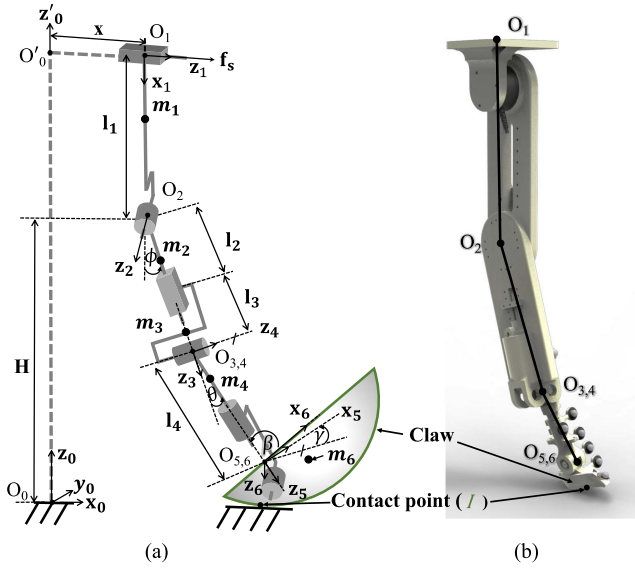


Fig. 3. 3-D dynamic model of the hoof. (a) Kinematic diagram. (b) 3-D model of the system. The fetlock, pastern, and coffin joints are illustrated in terms of their angles $\theta$, $\gamma$, and $\beta$ for simplicity.

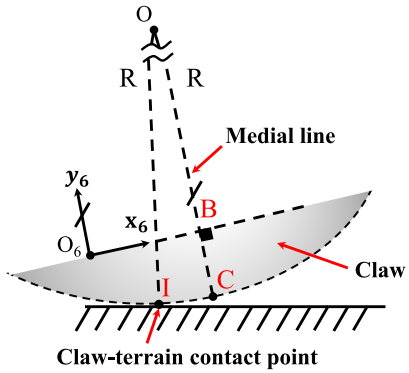


Fig. 4. Lateral view of the model of the claw. $\{0_6\}$ is the frame already defined in Fig. 3. $I$ is the contact point between the claw and the terrain. The medial line is parallel to the $y_6$-axis. This medial line also divides the claw in two halves. $\|\mathbf{BC}\|$ is the height of the claw. $\|\mathbf{O_6B}\|$ is the distance between $\{0_6\}$ and $B$ along $x_6$. For modeling the claw, we are assuming that it is a segment of a circle of radius $R$.

11) Due to the relatively low speed at the joints and low variation of the height, the links are represented as a one-point mass, and the gravitational potential energy is considered negligible compared to the other forces in the system.
12) All the springs have a virtual damper in parallel; consequently, the system contains dampers at $O_2$'s joint, prismatic joint between $O_2$ and $O_{3,4}$, roll, yaw, and pitch denoted $c_\phi$, $c_{23}$, $c_\theta$, $c_\gamma$, and $c_\beta$, respectively.

*1) Model of the Robotic Hoof:* The robotic hoof consists of the fetlock, pastern, and coffin revolute joints presented in Fig. 2. As stated earlier, in this article, it is considered that $\theta$, $\gamma$, and $\beta$ denote the yaw, roll, and pitch of the hoof, respectively. Each joint consists of a spring and a damper in parallel. Yaw and pitch have the same origin $O_{5,6}$, and each branch of the hoof is comprised of the phalanges and the claw, which have been represented with links.

These links and angles are illustrated in Fig. 3. The model was obtained using the parameters summarized in Tables I and II with the Khalil and Dombre variation of the Denavit–Hartenberg convention.

The coordinates of the contact point $I$ in the frame $(O_6, \boldsymbol{x}_6, \boldsymbol{y}_6, \boldsymbol{z}_6)$ were defined using trigonometry as follows:

$$\mathbf{O_6I}.\mathbf{x_6} = \|\mathbf{O_6B}\| - R\sin(0.5\pi + \phi - \beta) \quad (1)$$

$$\mathbf{O_6I}.\mathbf{y_6} = \|\mathbf{BC}\| + R\cos(0.5\pi + \phi - \beta) - R \quad (2)$$

TABLE I
VARIABLES AND PARAMETERS OF THE SYSTEM

| Variables / Parameters | Symbol |
|---|---|
| Time | $t$ |
| Energy needed to slide the hoof | $E$ |
| Velocity of $O_1$ [1⋆] | $v_1$ |
| Angle between the claw and the phalanges(Pitch) | $\beta$ |
| Half the angle between the claws(Roll) | $\theta$ |
| Angle between the claw and the $x_0$ axis(Yaw) | $\gamma$ |
| Length of $Link$ 1 | $l_1$ |
| Length of $Link$ 2 plus the length of $Link$ 3 | $l_{23}$ |
| External force applied at $O_1$ in the $x_0$ direction | $f_s$ |
| Friction force between the ground and the claw's sole | $\mathbf{F}_r$ |
| Position of the contact point claw - ground[2⋆] | $\mathbf{r}_I$ |
| Distance between $O_6$ and the medial line | $\|\mathbf{O_6B}\|$[3⋆] |
| Height of the claw | $\|\mathbf{BC}\|$[3⋆] |
| Radius of the circle's segment used for modeling the claw | R[3⋆] |
| Internal state vector of the friction force[4⋆] | $\mathbf{z}_i$ |
| Friction model stiffness coefficient | $\sigma_0$ |
| Friction model microdamping coefficient | $\sigma_1$ |
| Friction model macrodamping coefficient | $\sigma_2$ |
| Stribeck velocity | $v_s$ |
| Static friction coefficient | $\mu_s$ |
| Kinetic friction coefficient | $\mu_c$ |
| Angle at $O_2$ (it is between the foot and $-\mathbf{z}_0$) | $\phi$ |
| Stiffness of the joint at $O_2$ | $k_\phi$ |
| Stiffness of the Prismatic joint that is between $O_2$ and $O_{3,4}$ | $k_{23}$ |
| Stiffness at the pitch (antagonistic spring) | $k_\beta$ |
| Stiffness at the roll (inter-digital spring) | $k_\theta$ |
| Stiffness at the yaw (rotational spring) | $k_\gamma$ |
| Damping coefficient of the joint at $O_2$ | $c_\phi$ |
| Damping coefficient at the prismatic joint | $c_{23}$ |
| Damping coefficient for the roll | $c_\theta$ |
| Damping coefficient for the pitch | $c_\beta$ |
| Damping coefficient for the yaw | $c_\gamma$ |
| Height of $O_2$ | $H$ |
| Mass of $Link$ $i$[5⋆] | $m_i$ |
| Mass of the claw ($Link$ 6) | $m_6$ |
| Acceleration of the center of mass of $Link$ $i$[5⋆] | $\ddot{\boldsymbol{G}}_i$ |
| Acceleration of the center of mass of the claw | $\ddot{\boldsymbol{G}}_6$ |
| Compliance level at the roll | $C_\theta$ |
| Compliance level at the pitch | $C_\beta$ |
| Compliance level at the yaw | $C_\gamma$ |

[1⋆] For the simulation, $v_1$ is constant, but for the experiments, it is the speed of the $XY$ stage.
[2⋆] $r_I$ is defined with respect to the global inertial frame $O_0$. Additionally, $I$ is linked to the claw.
[3⋆] These parameters are illustrated in Fig. 4.
[4⋆] When the pitch and yaw are locked (clamped), the dimension of this vector is $1 \times 1$; otherwise, it is $2 \times 1$ due to the components in $x$ and $y$ of the friction force.
[5⋆] $i = 2, 3, 4$, which corresponds to Link 2, Link 3, and Link 4.

TABLE II
DENAVIT–HARTENBERG PARAMETERS OF THE HOOF

| i | $a_i$ | $\alpha - i$ | $b_i$ | $\theta - i$ |
|---|---|---|---|---|
| 0 | 0 | 0 | $H + l_1$ | $-\pi/2$ |
| 0' | 0 | $-\pi/2$ | $x$ | $\pi/2$ |
| 1 | $l_1$ | $\pi/2$ | 0 | $\pi/2 + \phi$ |
| 2 | 0 | $\pi/2$ | $l_{23}$ | $\pi/2$ |
| 3 | 0 | $\pi/2$ | 0 | $\theta$ |
| 4 | 0 | $-\pi/2$ | $l_4$ | $-\pi/2 + \gamma$ |
| 5 | 0 | $-\pi/2$ | 0 | $\pi/2 - \beta$ |

where $\|\mathbf{O_6B}\|$ is the distance between $O_6$ and the medial point of the claw, $\|\mathbf{BC}\|$ is the height of the claw, R is the radius of the claw defined in assumption 5). These parameters are illustrated in Fig. 4.

*2) Equation of Motion:* The variables and parameters utilized are described in Table I. The dynamics of the system were derived using the following extended version of the Euler–Lagrange equation:

$$\frac{d}{dt}\left(\frac{\partial L}{\partial \dot{\boldsymbol{q}}'}\right) - \frac{\partial L}{\partial \boldsymbol{q}'} = \boldsymbol{Q}'^{T} \tag{3}$$

where $L$ is the Lagrange, which is the difference between the kinetic and potential energies of the system; $\boldsymbol{q}'$, the state vector of the system, is equal to $\boldsymbol{q}' = [l_{23} \;\; \phi \;\; \theta \;\; \gamma \;\; \beta]$; $\dot{\boldsymbol{q}}'$ is its time derivative; and $\boldsymbol{Q}'$ is the nonconservative generalized forces vector that is calculated using the virtual work.

The nonconservative forces are friction force at the tip of the claw and all the damping forces.

The kinetic energy of the system comprises that from the masses $m_2$, $m_3$, $m_4$, and $m_6$. On the other hand, the potential energy is the summation of the energy stored in the springs at $O_2$ ($\phi$), prismatic joint between links 2 and 3, roll ($\theta$), yaw ($\gamma$), and pitch ($\beta$) denoted $k_\phi$, $k_{23}$, $k_\theta$, $k_\gamma$, and $k_\beta$, respectively.

*3) Friction Model:* In our previous work [14], we noticed a variation on the slip resistance due to the dynamics of the robotic hoof. Though the friction coefficients remained the same across the experiments (the materials in contact were the same), the robotic hoof exhibited a stick and slip behavior. Consequently, to model this dynamic behavior of the friction force $\boldsymbol{F}_r$, the LuGre friction model was chosen for the numerical simulation in this article. For the dynamic change of $\boldsymbol{F}_r$, this friction model employs several parameters. This model combines the Dahl model with the Stribeck effect [26]. This approach models the interaction between the irregularities of two contacting surfaces as elastic bristles. The average deflection of these bristles is the internal state $z_i$ of the model.

Due to the roll and yaw, the claw can move in the $(0_6, x_0, y_0)$ plane. Therefore, the $j$th component of the internal state, Stribeck effect, and friction force are defined by

$$\dot{z_{i,j}} = \dot{r}_{P,j} - \sigma_0 \frac{|\dot{r}_{P,j}|}{g(v)_j} z_{i,j} \tag{4}$$

$$g(v)_j = N\left[\mu_{c,j} + (\mu_{s_j} - \mu_{c_j}) e^{-|\dot{r}_{P,j}/v_s|^2}\right] \tag{5}$$

$$f_{r,j} = \sigma_0 z_{i,j} + \sigma_1 \dot{z_{i,j}} + \sigma_2 \dot{r}_{P,j} \tag{6}$$

where $\sigma_0$ is the stiffness, $\sigma_1$ is the microdamping, $\sigma_2$ is the macrodamping (viscosity coefficient), $v_s$ is the Stribeck velocity [27], and $N$ is the normal force [28]. Therefore, the friction force in the $j$th direction, $f_{r,j}$, is the summation of the resultant forces produced by bending the spring-like bristles [presented as the first and second terms in (6)] and the viscous friction [represented by the last term in (6)] [29]. Additionally, because the ground is our inertial frame, $\dot{r}_{I,j}$ is the relative speed between the two surfaces.

*4) Geometrical Constraint:* Since it is assumed that the claws are always in contact with the ground, the vertical component of $\boldsymbol{r}_I$ is equal to zero. Then, the geometrical constraint that keeps the vertical distance between $O_2$ and $I$ equal to $H$ is defined by

$$\begin{aligned} 0 = {} & [(I_x \cos\beta - I_y \sin\beta - d_6)\cos\theta \\ & - \sin\gamma \sin\theta (I_y \cos\beta + I_x \sin\beta) - l_{23}]\cos\phi \\ & + \sin\phi \cos\gamma (I_y \cos\beta + I_x \sin\beta) + H. \end{aligned} \tag{7}$$

From this equation, $l_{23}$ is cleared and substituted in the system of equations (3). This reduces the state variable vector to

$$\boldsymbol{q} = \begin{bmatrix}\phi & \theta & \gamma & \beta\end{bmatrix}^T. \tag{8}$$

In the end, the dynamic model was solved by numerical integration using the following equation:

$$\boldsymbol{R}\dot{\boldsymbol{s}} = \boldsymbol{A} \tag{9}$$

where

$$\mathbf{R} = \begin{bmatrix} \mathbf{I}_n & \mathbf{O}_{n\times n} & \mathbf{O}_{n\times j} \\ \mathbf{O}_{n\times n} & \mathbf{M}_{n\times n} & \mathbf{B}_{n\times j} \\ \mathbf{O}_{j\times n} & \mathbf{O}_{j\times n} & \mathbf{I}_j \end{bmatrix}$$

$$\dot{\mathbf{s}} = \begin{bmatrix}\dot{\mathbf{q}} & \ddot{\mathbf{q}} & \dot{\mathbf{z}}_i\end{bmatrix}^T$$

$$\boldsymbol{A} = \begin{bmatrix}\dot{\boldsymbol{q}}_{0,n\times 1} & \boldsymbol{Q}_{e,n\times 1} & \boldsymbol{H}_{j\times 1}\end{bmatrix}^T.$$

$\mathbf{I}$ is the identity matrix, $n$ is the number of state variables in $\mathbf{q}$, $\mathbf{O}$ is the zero matrix, $j$ is the number of components on the friction internal state vector $\mathbf{z}_i$, $\mathbf{M}$ comprises the effects of the mass, $\mathbf{B}$ includes the microdamping coefficients of the friction model, $\ddot{\mathbf{q}}$ is the second time derivative of the new state vector, $\dot{\mathbf{z}}_i$ is the first derivative of the internal state vector of the friction force model, $\dot{\mathbf{q}}_0$ are the initial conditions, $\mathbf{Q}_e$ is the vector of forces that includes those from the dampers and springs at the joints, and those from the spring-like bristles from the friction model and the viscous friction, and $\mathbf{H}$ is the vector of $\dot{\mathbf{z}}_i$ defined by (4).

In this article, we used four compliance levels (0, 1, 2, and 3) for the yaw, roll, and pitch, which are summarized in Table III. For facilitating the analysis, the compliance-level notation at the joint levels is $C_j^i$, where $i = 0, 1, 2, 3$ is the compliance level and $j = \gamma, \theta, \beta$ indicates where the compliance is applied. $\gamma$, $\theta$, and $\beta$ correspond to the yaw, roll, and pitch, respectively. Level 0 denotes no compliance (locked joint), while level 3 is the most compliant. The stiffness of the springs for these levels was chosen based on the commercially available springs.

TABLE III
COMPLIANCE LEVEL OF THE JOINTS

| Compliance Level | Stiffness[1*] | | |
|---|---|---|---|
| | **Yaw** $k_\gamma$[N m/rad] | **Roll** $k_\theta$[N/m] | **Pitch** $k_\beta$[N/m] |
| 0 | $\infty$ | $\infty$ | $\infty$ |
| 1 | 0.369 | 550 | 570 |
| 2 | 0.136 | 150 | 150 |
| 3 | 0.127 | 50 | 90 |

[1*] For simplicity, the compliance levels are defined in terms of the inverse of the stiffness of the springs $k_\gamma$, $k_\theta$, and $k_\beta$ for the yaw, roll, and pitch, respectively.

## III. METHODOLOGY

The effects of the embodiment of the hoof are analyzed in terms of the external energy required to slide the hoof 6 cm over a hard terrain. Consequently, the analysis also takes into account the energy dissipated due to the friction force and the variation on the potential energy stored in the spring-like mechanisms, where the higher the value of the external energy, the higher the slip resistance. This allows us to determine the most significant compliance combinations across all joints that improve the slip resistance of the robotic hoof and to understand the individual contribution of its joints on the slip resistance. It has to be pointed out that since the material of the pads and the terrain were the same for all the experiments, there is no source of variation for the coefficient of friction.

Additionally, a low slip speed of $v_1 = 10$ mm/s was chosen in simulations and experiments to study how the passive dynamics of the hoof improve slip resistance with minimum need for active control action to stop slippage.

### A. Numerical Simulation

Utilizing the simulation parameters summarized in Table IV, we have tested our mathematical model of the hoof for different compliance levels, presented in Table III, using "ode23" in MATLAB R2017b. Since the system reaches its steady state after 2 s and the slip resistance depends on the compliance level of the joints, this analysis comprises until the claw has moved 0.0188 m.

A high-performance computing facility (a general-purpose mixed architecture cluster with about 25 000 cores) was employed due to the size and complexity of the numerical simulation. There are some compliance combinations, whose simulation was computationally expensive. Therefore, the number of trials for each compliance level is different, and they are summarized in Table V.

Due to the lack of research regarding the compliance of the goat's hoof joints, it has to be pointed out that this article mainly utilizes the simulation results to obtain the profile of the energy required to slide the hoof for the compliance levels of each joint summarized in Table III.

*1) Energy Analysis:* Before calculating the energy, the external force needed to move the hoof at $O_1$ at the constant speed $v_1$ was found as follows:

$$\boldsymbol{F}_{\text{ext}} = m_2\ddot{\boldsymbol{G}}_2 + m_3\ddot{\boldsymbol{G}}_3 + 2m_4\ddot{\boldsymbol{G}}_4 + 2m_6\ddot{\boldsymbol{G}}_6 - 2\boldsymbol{F}_r \quad (10)$$

TABLE IV
SIMULATION PARAMETERS

| System | Variables | Values |
|---|---|---|
| External Force applied at $O_1$ | $v_1$ | 0.01[m/s] |
| Friction Model | $\sigma_0$ | 8[N/m] |
| | $\sigma_1$ | 0.089[N s/m] |
| | $\sigma_2$ | 0.05[N s/m] |
| | $v_s$ | $1 \times 10^{-3}$[m/s] |
| | $\mu_s$ | 0.3 |
| | $\mu_c$ | 0.2339 |
| Rigid Leg | $k_\phi$ | 100[N m/rad] |
| | $c_\phi$ | 10[Kg/s] |
| | $H$ | 0.275[m] |
| Prismatic Joint | $k_{23}$ | 374[N/m] |
| | $c_{23}$ | 7[Kg/s] |
| Hoof[1*] | $c_\theta$ | 0.7[Kg/s] |
| | $c_\gamma$ | 0.7[Kg/s] |
| | $c_\beta$ | 0.7[Kg/s] |
| | $\|\mathbf{O_6B}\|$ | 0.0241[m] |
| | $\|\mathbf{BC}\|$ | 0.043[m] |
| | $R$ | 0.0775[m] |
| | $l_1$ | 0.014[m] |
| | $l_4$ | 0.0859[m] |
| | $m_2$ | 0.0672[Kg] |
| | $m_3$ | 0.0162[Kg] |
| | $m_4$ | 0.0081[Kg] |
| | $m_6$ | 0.0065[Kg] |
| Initial Conditions | $\phi_0$ | 18° |
| | $\theta_0^{2*}$ | $[4° - 11°]$ |
| | $\gamma_0^{2*}$ | $[4° - 21°]$ |
| | $\beta_0^{2*}$ | $[91° - 99°]$ |
| | $zi_{x,0}$ | $1 \times 10^{-8}$[m] |
| | $zi_{y,0}$ | $1 \times 10^{-8}$[m] |
| | $\dot{\phi}_0$ | $1 \times 10^{-5}$[rad/s] |
| | $\dot{\gamma}_0$ | $1 \times 10^{-5}$[rad/s] |
| | $\dot{\theta}_0$ | $1 \times 10^{-5}$[rad/s] |
| | $\dot{\beta}_0$ | $1 \times 10^{-5}$[rad/s] |
| Time step | $\Delta t$ | 0.005[s] |

[1*] The value of the compliance level of the joints is described in Table III
[2*] Interval used for defining the initial condition of the angles.

TABLE V
NUMBER OF TRIALS FOR THE NUMERICAL ANALYSIS

| Compliance Level | Degree of freedom | | |
|---|---|---|---|
| | **Yaw** | **Roll** | **Pitch** |
| 0 | 483 | 290 | 298 |
| 1 | 235 | 476 | 242 |
| 2 | 138 | 118 | 247 |
| 3 | 152 | 124 | 221 |

where $m_2$, $m_3$, $m_4$, and $m_6$ are the masses and $\ddot{\boldsymbol{G}}_2$, $\ddot{\boldsymbol{G}}_3$, $\ddot{\boldsymbol{G}}_4$, and $\ddot{\boldsymbol{G}}_6$ are the accelerations of the center of mass of the links of the system. The later were obtained by solving (9). However, the external force, $f_s$, is only moving $O_1$ along $x_0'$. As a consequence, $f_s$ is the $x$ component of $\boldsymbol{F}_{\text{ext}}$. Then, the energy

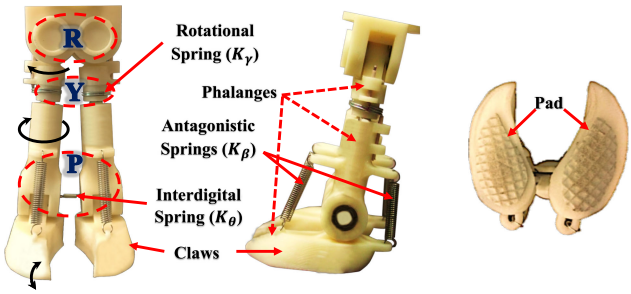


Fig. 5. Abstraction of the goat hoof. It comprises (a) the variable compliance joints fetlock joint (R), pastern joint (Y), coffin joint (P), phalanges (with their respective rotation illustrated with the black arrows), claws, and springs changed during the experiments, and (b) pad.

$E$ due to $f_s$ was determined using

$$E = \int_{t_0}^{t_1} f_s(t) v_1 dt. \tag{11}$$

The analysis of these data comprises studying the individual and pairwise impact of the change of the compliance level of each joint on the energy.

### B. Mechanical Design

We used a multibody compliant robotic hoof inspired by the goat for experiments. Our aim was to test the hypothesis that the passive dynamics of the hoof may be making a significant contribution to improving slip resistance.

The hoof was constructed using a three-dimensional (3-D) printer with ABSplus as model material. Its height is 11 cm, and the length of the claw is 5.5 cm. As illustrated in Fig. 5(a) and (b), the hoof is comprised of three joints.

The fetlock joint (roll) consists of four identical stainless steel flanged Metal Radial Ball Bearings for the lateral movement of the claws. To emulate the interdigital ligament of the hoof that defines the compliance of this joint, there is an interdigital spring $k_\theta$ from Lee Spring Limited. Depending on the compliance level, $k_\theta$ can have the values presented in Table III.

The pastern joint (yaw) was built using three stainless steel NMB Metal Radial Ball Bearings. To define the compliance of the joint and the default position of the tip of the claw, the joint comprises a torsional spring with stiffness $k_\gamma$ and free position ends of 90° from Lee Springs Limited. The values of $k_\gamma$ for the four compliance levels are summarized in Table III.

The coffin joint (pitch) is made of two ball bearings identical to those used in the fetlock joint. The compliance of this joint is set by two similar antagonistic springs located at the front and back of the claw. The stiffness $k_\beta$ of these antagonistic springs is presented in Table III.

In the end, the profile of the claw was taken from an adult Ecuadorian common goat (Capra Hircus) [30], [31], while the curved pad was made of ethylene-vinyl acetate (see Fig. 5).

### C. Experimental Protocol

For the experimental analysis, the data for sliding the hoof 6 cm for 64 joint compliance-level combinations were collected.

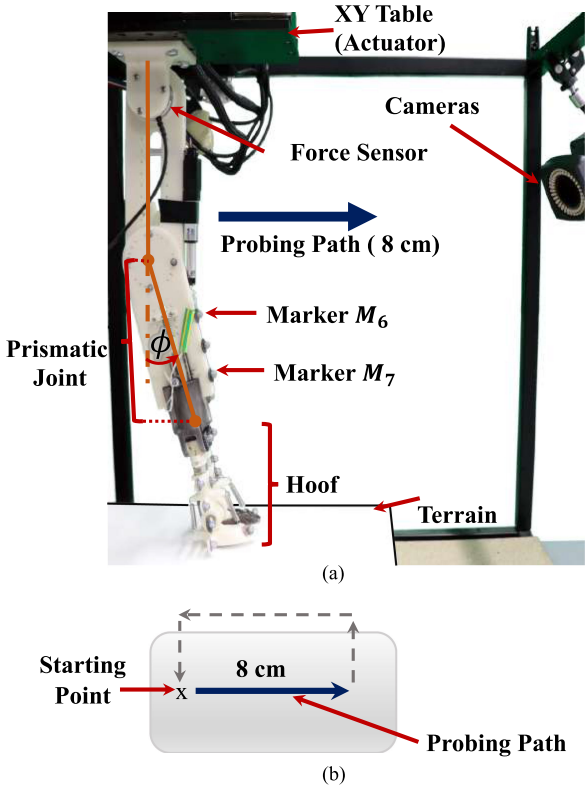


Fig. 6. Experiment setup. (a) Hoof was attached through the prismatic joint to the rigid leg. This leg was secured to the stage through the force sensor. Four cameras together with reflective markers were used to track the position of the components of the hoof and the prismatic joint. The position of the markers $M_6$ and $M_7$ are used for defining the midline from the leg to calculate $\theta$. (b) Top view of the probing path followed by the $XY$ stage for each trial. The starting position is marked with an "x."

These combinations result from combining all the compliance levels of the joints presented in Table III. It has to be clarified that for achieving compliance level 0, the respective joint was clamped.

The experiment for each combination was comprised of 26 trials with an individual duration of 8 s. This trial length is justified by the fact that 8 s multiplied by $v_1$ gives a maximum claw displacement of 8 cm. This displacement avoids having missing data (especially from the cameras illustrated in Fig. 6), and 8 s is enough for having a minimum claw displacement of 6 cm for all the combinations.

On the other hand, the length of the simulation trial is different from that of the experiment because the simulation for some combinations is computationally expensive, and we have limited access to the high-performance computing facility.

The overall experimental setup is depicted in Fig. 6. The AEROTECH XY stage-type ANT130-160-XY-25DU-XY-CMS moved the rigid leg at the constant speed of $v_1$. In the design, $\phi$ was set to 18°, which was the value used in the simulations. A prismatic joint links the rigid leg to the hoof. This prismatic joint contains a compression spring $k_{23} = 364$ N/m from LeeSpring Limited for passively changing the normal force. The tested surface was P40 sandpaper covered with plain white paper for obtaining a hard terrain with calibrated roughness (defined by

the grit of the sandpaper) and for avoiding damaging the hoof. Fig. 6(b) presents the 8-cm path followed by the $XY$ stage during each trial.

To quantify the energy, the measured variables were the stage's current and position, hoof position, and force at joint $O_1$. Stage's parameters were obtained from its Ensemble controllers. The force was measured at the end of the rigid leg using the MINI40 SI-40-2 sensor with a sampling frequency of 900 Hz. This information was gathered using LabView2016 from National Instruments. The VICON motion capture system comprised of reflective markers (diameter = 6.4 mm) and four VICON Bonita B10 cameras (200 frames/s, 1 megapixel) was used to capture the movement of the hoof. These data were collected at 200 samples/s. The cameras were placed in the front of the hoof, and three markers were attached to each object for tracking its position. The objects were the claws, the middle phalanges, the rigid leg, and the stage. Then, the VICON data acquisition process was carried out using MATLAB R2017b from MathWorks.

*1) Analysis of the Energy Required to Slip:* It starts by evaluating how the change of compliance level of each joint affects the energy required to slide the hoof. Then, pairwise comparison between two angles and the energy reveals the effects of the interaction between joints in the energy. Later, these results are complemented utilizing statistical analysis. In general, these data were analyzed using MATLAB R2018b, and the Statistics together with the Machine Learning Toolbox were utilized for the Statistical Analysis.

The energy required to slide the feet was obtained from the integration of the power consumed by the motors. This power was calculated as [32]

$$p_{\text{out}} = 3\text{Bemf}I \tag{12}$$

where the back electromotive force constant, Bemf, is measured in volts, and it is defined by $\text{Bemf} = 9\dot{r}_{D,x_0}$ [33]. $I$ is the rms current in amperes. Then, the energy $E$ was obtained by

$$E = \int_{t_0}^{t_1} p_{\text{out}}(t)dt \tag{13}$$

where $dt = 5 \times 10^{-3}$.

For the statistical analysis, data were normalized. Then, the one-sample Kolmogorov–Smirnov test revealed that the data were not normally distributed. To evaluate if the average energy of the combinations belongs to different distributions, the Kruskal–Wallis statistical significance test with the Bonferroni correction was used. To conclude, the combinations with the highest and lowest energy values were determined using the Mann–Whitney U test at 1% significance level.

*2) External Force and Kinematic Relationships Determining Slip Resistance:* The position of the hoof's markers from $M_1$ to $M_5$ [see Fig. 2(a)–(c)] and the position of the markers $M_6$ and $M_7$ of the prismatic joint [see Fig. 6(a)] were utilized to calculate the angles using the following equations:

$$\theta = \arccos \frac{\mathbf{M_1M_3} \cdot \mathbf{M_6M_7}}{\|\mathbf{M_1M_3}\| \, \|\mathbf{M_6M_7}\|} \tag{14}$$

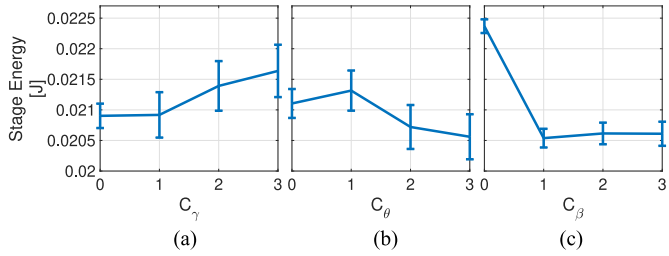


Fig. 7. Simulation results. Energy required to slide the hoof 0.0188 m across all the compliance levels at the (a) yaw $C_\gamma$, (b) roll $C_\theta$, and (c) pitch $C_\beta$.

$$\gamma = \arctan \frac{\mathbf{M_2M_{5y_0}}}{\mathbf{M_2M_{5x_0}}} \tag{15}$$

$$\beta = \arccos \frac{\mathbf{M_3M_1} \cdot \mathbf{M_4M_5}}{\|\mathbf{M_3M_1}\| \, \|\mathbf{M_4M_5}\|}. \tag{16}$$

To facilitate the analysis, the energy values for the combinations have been grouped into high, medium, and low energy value scenarios. These groups comprise the combinations in the top, medium, and bottom quintiles of the energy.

The analysis of the external force and the contribution of each joint on the slip resistance of the hoof comprises the study of the following:

1) the pairwise behavior of the angles;
2) the statistics of the external force;
3) the typical time profile of the raw data of the forces and angles;
4) the average and standard error of the raw experimental data of the angles;
5) the probability distribution of the angles of the joints for all the combinations in the high, medium, and low energy scenarios.

## IV. Results

The aims of this article are to determine the most significant compliance combinations across joints in the hoof (shown in Table III) to improve slip resistance, and to investigate the contribution of each joint to improve slip resistance.

### A. Analysis of the Energy Required to Slip

The simulation results in Fig. 7 show the variation of stage energy across different compliance levels in the yaw ($C_\gamma$), pitch ($C_\beta$), and roll ($C_\theta$). In general, it can be noticed that the stage energy increases when $C_\gamma$ increases and $C_\theta$ decreases. This indicates that there is a causality between slip resistance and compliance level of the hoof joints.

The simulation results also illustrate that low compliance for $C_\beta$ gives higher slip resistance. It should be noticed that the simulation was done using a single-point contact model. However, the real hoof involves a complex contact geometry. Therefore, detailed experiments are needed to verify details of the causality between the slip resistance and the compliance of the joints.

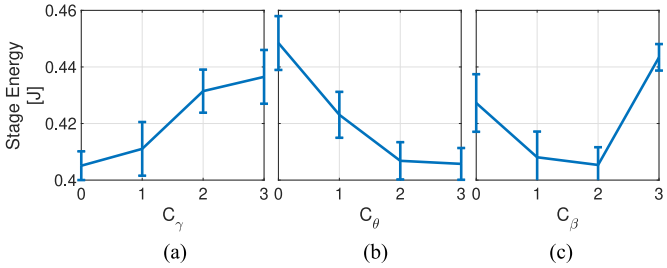


Fig. 8. Experiment results. Energy required to slide the hoof 0.06 m across all the compliance levels at the (a) yaw $C_\gamma$, (b) roll $C_\theta$, and (c) pitch $C_\beta$.

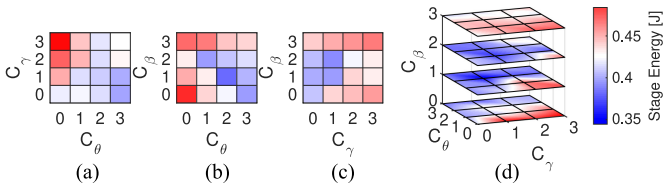


Fig. 9. Experiment results. Pairwise comparison of the energy required to slide the hoof: (a) $C_\gamma$ against $C_\theta$, (b) $C_\beta$ against $C_\theta$, and (c) $C_\beta$ against $C_\gamma$. (d) 3-D plot of the stage energy across the compliance levels of the three joints. To highlight the compliance-level combinations with a higher or lower expected energy value than the baseline (stiff combination, $E(C_\gamma^0, C_\theta^0, C_\beta^0)$), the former are represented using an scaled red color, while the latter uses an scaled blue color. Additionally, the center of the bar color (white color) denotes the energy of the baseline.

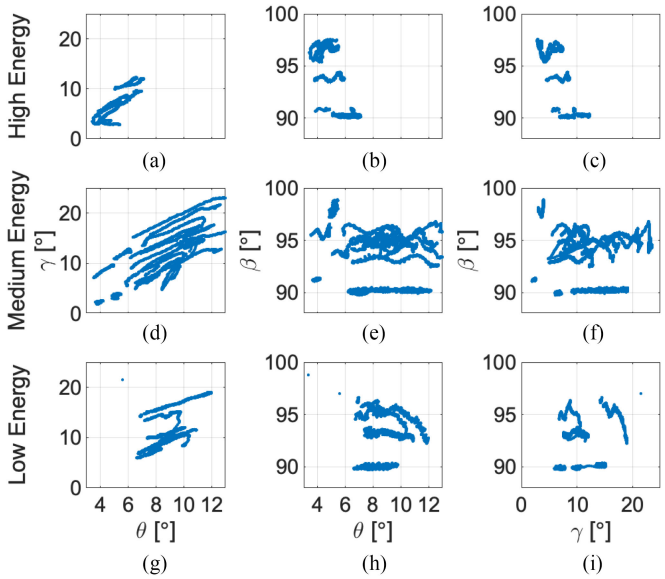


Fig. 10. Experiment results. Pairwise comparisons of the evolution of the angles of the hoof: *column 1:* $\gamma$ against $\theta$; *column 2:* $\beta$ against $\theta$; and *column 3:* $\beta$ against $\gamma$. The high, medium and low energy scenarios contain those combinations with an energy value in the top, medium, and bottom quintiles of the range of the experimental data.

Fig. 8 presents the experimental results for the variation of the stage energy for different levels of $C_\gamma$, $C_\theta$, and $C_\beta$. They show a similar pattern seen in the simulation results. We can notice that the stage energy is high when $C_\gamma$ is high and $C_\theta$ is low. The main difference between simulations and experiments is that in experiments, higher $C_\beta$ gives higher slip resistance.

On the other hand, the three joints of the hoof interact not only with the environment, but also with one another. Therefore, we need to study the interaction effect among joints on the hoof slip resistance. We performed a pairwise analysis, as shown in Fig. 9. This figure shows the stage average energy across all the compliance levels $C_\gamma$, $C_\beta$, and $C_\theta$ by pairs and across all the joints.

The pairwise comparison of $C_\theta$ and $C_\gamma$ and the interactions between compliance across the three joints and the stage energy reveal that the stage energy is higher for high compliance levels of $C_\gamma$ and low compliance levels of $C_\theta$. This means the interdigital ligaments should be stiff, while the pastern joint ($C_\gamma$) should be compliant to increase slip resistance.

Results of stage energy for $C_\beta$ against $C_\theta$, $C_\beta$ against $C_\gamma$, and the 3-D plot of the stage energy across the compliance of the three joints demonstrate that, in general, higher compliance at the pitch ($C_\beta$) leads to higher slip resistance.

These results are corroborated by the single-sided comparisons ($p < 0.05$, Mann–Whitney U-test at 1% significance level with Kruskal–Wallis with Bonferroni correction). These results show that the combinations with the highest slip resistance that present up to $\approx 20\%$ increase of energy by compared to the baseline (stiff combination) have a compliant $C_\gamma$ and a stiff roll ($C_\theta^0$).

Conversely, the statistical analysis ($p < 0.05$, Mann–Whitney U-test at 1% significance level with Kruskal–Wallis with Bonferroni correction) also shows that the combinations that required the lowest energy to slide the hoof are comprised of a low $C_\gamma$ and high $C_\theta$.

In summary, most of the high-energy combinations comprise $C_\gamma,\ C_\beta > 0$, while $C_\theta$ is stiff. These findings confirm the importance of having the right compliance levels at the joints for increasing the slip resistance of the hoof.

### B. Force and Kinematic Relationships Determining Slip Resistance

To understand the kinematic implications of passive contact force management to increase slip resistance, we analyzed the statistics of the contact forces and the variation of $\gamma$, $\beta$, and $\theta$.

So far, the energy results show that having $C_\gamma$ compliant and $C_\theta$ stiff improves the slip resistance of the hoof. Therefore, we need to understand how every angle and the magnitude of the external force needed to slide the hoof vary for the different compliance levels at the joints. For simplicity, the results are divided in the high, medium, and low energy scenarios that correspond to the set of combinations with energy in the top, medium, and bottom quintiles of the energy range from the experimental results, respectively.

It can be observed in Fig. 10 that the variation of the angles of the hoof for the high energy scenario is significantly lower than that in the other two scenarios. This may imply that the angle of the joints tends to reach some cyclic limit release that leads to punctuated contact forces like those in the ABS on automobiles.

Additionally, the results of Fig. 10 (column 1) show a linear relation between $\gamma$ and $\theta$. These results also establish a

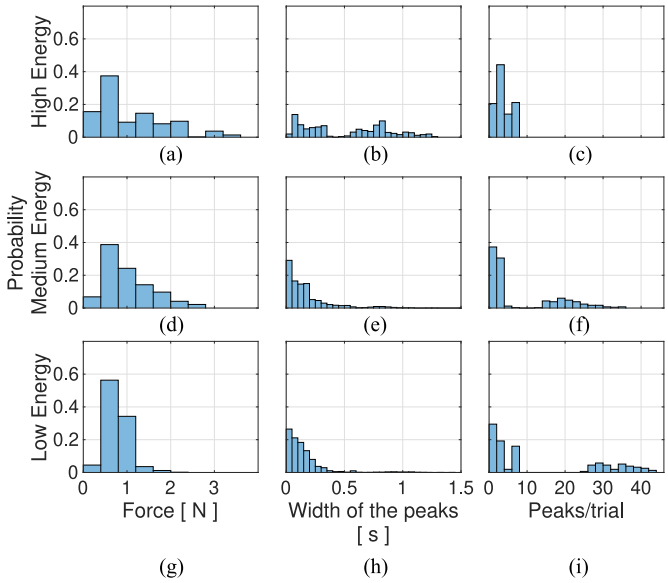


Fig. 11. Experimental results. Probability distribution of the *(column 1)* height of the peaks, *(column 2)* width of the peaks, and *(column 3)* number of peaks per trial of the magnitude of the external force, $\|\mathbf{F}_{\text{ext}}\|$, for the combinations in the *(row 1)* high, *(row 2)* medium, and *(row 3)* low energy scenarios.

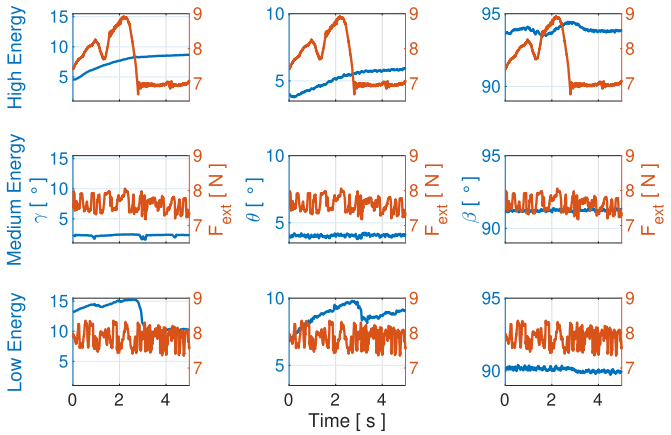


Fig. 12. Experiment results. Raw data of the external force, $\|\mathbf{F}_{\text{ext}}\|$, required to slide the hoof and behavior of the angle at the *(column 1)* yaw ($\gamma$), *(column 2)* roll ($\theta$), and *(column 3)* pitch ($\beta$) for the *(row 1)* high energy scenario, *(row 2)* medium energy scenario, and *(row 3)* low energy scenario. It has to be pointed out that for illustration purposes, the signals are only plotted for the first 5 s.

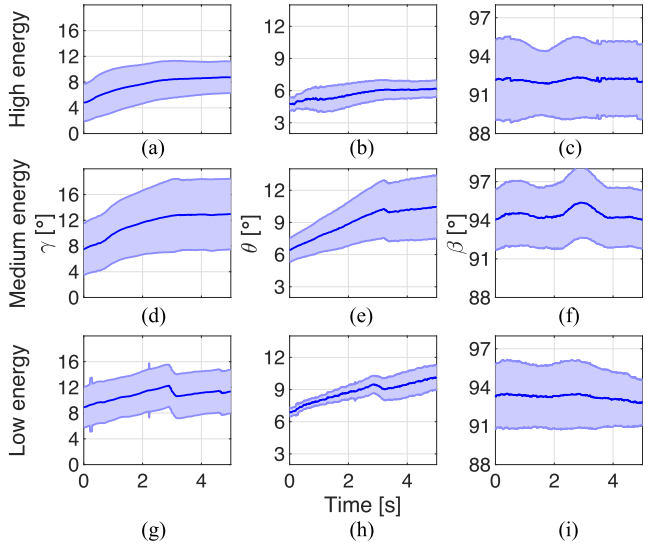


Fig. 13. Experiment results. Average and standard error of the raw experimental data of the evolution of the angles: $\gamma$ (column 1), $\theta$ (column 2), and $\beta$ (column 3) for all the combinations in the *(row 1)* high, *(row 2)* medium, and *(row 3)* low energy scenarios. For illustration purposes, the signals are only plotted for the first 5 s.

tendency of $\gamma$ and $\theta$ to move toward lower values (toward the bottom left corner of the plots) for the high energy scenario [see Fig. 10(a)]. The results of $\beta$ against $\theta$ and $\beta$ against $\gamma$ (see columns 2 and 3 in Fig. 10, respectively) present a similar relationship. These results reveal that the high energy scenario is comprised of compliant pitch combinations that exhibit an oscillating behavior and locked pitch combinations with $\beta \approx 90°$. The oscillating behavior is also noticed in the medium energy scenario, while this behavior is practically unnoticeable in the low energy scenario.

The consequence of this oscillating behavior observed in Fig. 10 is reflected in the statistics of external force $\|\mathbf{F}_{\text{ext}}\|$ shown in Fig. 11.

Fig. 11 reveals that the high stage energy required to slide the hoof corresponds to an increase in the probability of having slip resistance force peaks of higher magnitude and duration. This is also evident in the typical time profiles of the forces and angles shown in Fig. 12. The high energy scenario presents higher and low-frequency force peaks accompanied by more pronounced oscillatory behavior in the pitch together with asymptotically widening yaw and roll. Conversely, medium and low energy combinations present smaller and high-frequency force peaks.

Fig. 13 shows the average and standard error across all the trials for joint angle profiles. Particularly, column 1 in Fig. 13 reveals an asymptotically growing profile of $\gamma$ with lower standard error in the high energy scenario [see Fig. 13(a)] compared to that in medium and low energy scenarios. Another difference is that the expected value of $\gamma$ converges to $\approx 9°$ in the high energy scenario, while that of the others go beyond this value. Accordingly, Fig. 14 illustrates the probability distribution of the joint angles. In particular, column 1 shows that the higher the energy is, the lower the variability of $\gamma$ becomes. What stands out is that for the high energy scenario, the probability becomes shifted to the left, limited to $\gamma < 13.5°$, and only comprises combinations with $C_\gamma$ compliant.

Column 2 in Fig. 13 exhibits a relatively flat profile for $\theta$ in the high energy scenario. Nevertheless, $\theta$'s profile for the medium and low energy scenarios presents a quick small limit-release behavior. This is corroborated by column 2 in Fig. 14. What can be clearly seen is that for the high energy scenario, the histogram is left-skewed, with an upper limit of $\theta < 7.5°$, with an average value of $\theta \approx 5°$, and only comprises the lowest compliance level at the roll ($C_\theta$ stiff). This explains the flat profile of $\theta$ in Fig. 13(b). On the other hand, the probability distribution of $\theta$ for the medium energy scenario is unimodal

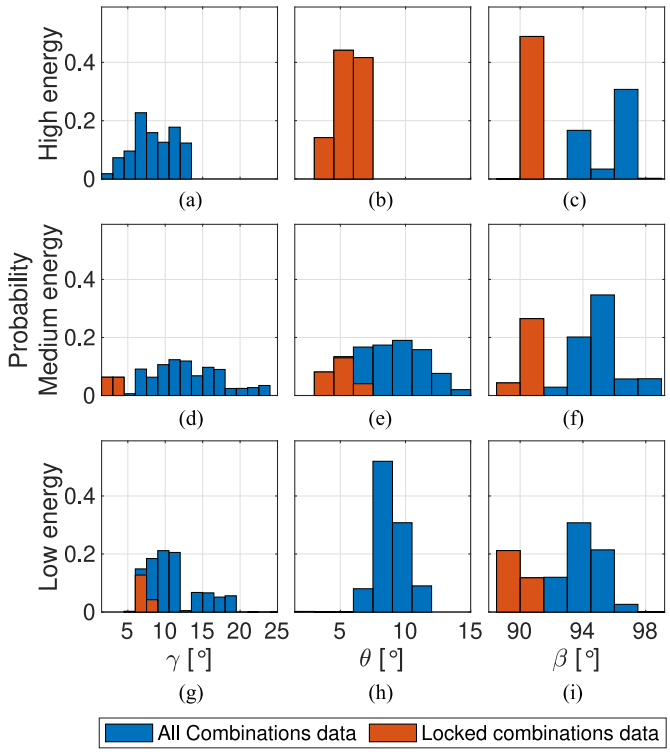


Fig. 14. Experiment results. Histogram of the probabilities of $\gamma$ (column 1), $\theta$ (column 2), and $\beta$ (column 3), for the combinations in the *(row 1)* high, *(row 2)* medium, and *(row 3)* low energy scenarios. The blue bars illustrate all the data, while the red bars highlight the probability distribution of the data from the stiff joints.

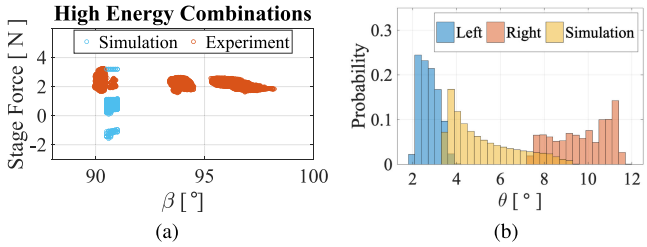


Fig. 15. Simulation and experimental results. (a) Stage force against $\beta$. (b) Histogram of the probability distribution of $\theta$ for a combination with compliant joints. Yellow bars illustrate the simulation data, while blue and orange bars correspond to the experimental results from the left and right claw, respectively.

with a high variability, whereas the probability distribution in the low energy scenarios is unimodal, with low variability, and only comprises compliant roll levels.

$\beta$'s time profile (see column 3 in Fig. 13) exhibits a uniform oscillatory behavior for the high energy scenario with an expected value $\approx 92°$. On the other hand, the profile of $\beta$ in the medium energy scenario has a variable oscillatory behavior, while the profile of the low energy scenario is relatively flat. It has to be pointed out that for the medium and low energy scenarios, the expected value of $\beta$ is $\approx 94°$. These are further validated by column 3 in Fig. 14. The bimodal probability distribution of the high energy scenario when the pitch is compliant [blue bars in Fig. 14(c)] agrees with the uniform oscillatory behavior observed in Fig. 13(c). In this case, the upper and lower bounds of the oscillation are defined by the two peaks in the histogram. In general, the medium energy scenario exhibits a bimodal probability distribution with high variability. This increase in the variability can be associated with the variable oscillatory behavior observed in Fig. 13(f).

In summary, for the high energy scenario, $\gamma$ shows a smooth asymptotic growth (opening digits) for a narrow flat variation of $\theta$ (stiff interdigital ligament). The cyclic limit-release behavior of $\beta$ (vertical movement of digits) is also smooth, which also contributes to improving the slip resistance of the hoof. In the medium energy scenario, even though $\gamma$ grows smoothly, there is a quick limit-release behavior of $\theta$ accompanied by a variable oscillating profile of $\beta$. On the other hand, the low energy scenario exhibits a quick limit-release behavior of $\gamma$ and $\theta$ and flat oscillations of $\beta$ making the hoof easier to slide.

## V. Discussion

As stated in the previous section, there is a difference between the simulation and experiments regarding the contribution of $C_\beta$ on the slip resistance. According to the latter, a higher $C_\beta$ gives higher slip resistance. This can be explained by the results presented in Fig. 15(a). It reveals that the variability of $\beta$ is higher for the experimental results than that for the simulation. This can be caused by the simplification of both the complex geometry of the pad and the contact between the hoof and the terrain. Furthermore, the vibrations on the structures of the components can also affect the variability of $\beta$.

Similarly, Fig. 15(b) states that another cause for the difference between the simulation and experiment results is that the behavior of the claws is not symmetric. The histogram of the probability distribution of $\theta$ is different for the left and right claws in the experiments. However, the simulation results demonstrate that the behavior of $\theta$ from the simulation is an average of that exhibited for the claws in the experiments. At some extent, it shows that the claws' symmetric behavior assumption in the mathematical model is not entirely unsuitable. The lack of symmetry in the experimental results can be a consequence of the pad's manual elaboration and adhesion to the claw.

Additionally, it has to be pointed out that though $\phi$ was set in the simulations and design of the robotic hoof to $18^\circ$, the experimental results show that given a trial with a variation of 0.69%, the expected value of $\phi$ is $14.36°$, and its range across trials is $\bar{\phi} \in [12° \ 16°]$. This can be explained by the hardware variability such as tolerances of the design or the elasticity of the 3-D printing material of the robotic hoof. Consequently, according to the experimental results, the variation of $\phi$ has a minimum effect on the slip resistance, while the simulation results establish a linear relationship that can be defined by $E = 0.3782\phi - 0.059$, where $\phi$ is in radians for a compliant combination.

On the other hand, the oscillatory dynamic behavior of the external force suggests that the robotic hoof presents an ABS-like behavior to increase its slip resistance. The ABS principle of vehicles based on the relation between the slip ratio of the wheel

and its tire's adhesion coefficient with the road surface for different asphalt conditions has been presented in [18]. The authors show that the tire-wet asphalt maximum adhesion coefficient is lower than that for tire-dry asphalt. Consequently, the braking force that can be applied to the wheel for wet asphalt conditions is smaller in magnitude and duration than the braking force that can be applied to the wheel for dry asphalt conditions [18]. This increments the time needed to brake when the asphalt is wet. Therefore, the high energy scenario resembles the dry asphalt conditions, while the low energy scenario resembles the wet asphalt conditions. This is highlighted in the growth of height and duration of the peaks of the external force with the increase in energy needed to slide the hoof observed in Fig. 12.

Results also reveal that having relatively higher compliance at the yaw ($C_\gamma$) and pitch ($C_\beta$) and lower compliance at the roll ($C_\theta$) increases the slip resistance of the hoof. This superior performance comes from the fact that due to these compliance levels, the interaction between the hoof and the terrain produces a smooth growth of $\gamma$, limited to values $< 13.5^\circ$, and a locked value of $\theta \approx 5^\circ$. This conducts to a cyclic smooth limit-release behavior at the pitch. This is a manifestation of hoof's ABS-like behavior that decreases the speed while avoiding skidding and losing balance. This is explained by the adaptability of the hoof to the small irregularities. This leads to the appearance of an additional braking behavior similar to the wedge braking used by skiers to brake in the snow. In the end, this leads to the manifestation of the ABS of vehicles at the hoof.

Similarly, in the medium energy combinations, $\gamma$ also asymptotically grows relatively smoothly. However, the quick limit-release behavior of $\theta$ is accompanied by vibrations observed in $\beta$'s profile, where the vibrations are not cyclic. This does not allow the hoof to effectively improve its slip resistance.

Conversely, the combinations with a low compliance level at the yaw ($\gamma$) and high compliance at the roll ($\theta$) present the lowest energy value. This is caused by the fact that the quick limit-release behavior at the yaw and the roll is accompanied by minimal oscillations at the pitch ($\beta$). Therefore, the dynamic behaviors of the hoof that reduce the speed mentioned in the previous paragraph cannot manifest in this case. This result also implies that the contribution of the lateral slip dissipation is low for improving the slip resistance.

Moreover, though the dynamics of the joints of the biological hoof differ from their corresponding robotic counterpart, which makes it difficult to conclude on the dynamics of the biological hoof, the results of this study agree with the overall energy-absorbing behavior of the hoof found in real goats [8]. According to our results, the best compliance combinations across the joints increase the energy required to slide the hoof by $\approx 20\%$ compared to that of the baseline (stiff combination). Therefore, the robotic hoof can give an insight into the dynamics of the biological hoof. This implies that the physical parameters of the robotic hoof can be isolated and studied. These studies are difficult to implement with real goats due to the complexity of their natural habitat and the invasive methods used to monitor parameters in animals that can alter their normal behavior.

## VI. Conclusion

This article, for the first time using a dynamic model and experimental results, investigated the role of the passive dynamics of a biologically inspired goat robotic hoof on the slip resistance. This article showed that having compliant yaw and pitch and a stiff roll could increase the energy required to slide the robotic hoof by $\approx 20\%$ compared to the stiff combination. Compliant yaw and pitch allow the system to interact with the irregularities of the terrain to generate oscillations in the pitch. This leads to the manifestation of ABS-like behavior in the robotic hoof that improves the slip resistance. Therefore, it can be stated that the coffin (pitch) and pastern joints (yaw) of the hoof play an important role on the slip resistance, while the effect of the fetlock joint (roll) is minimal. The latter allows robotic hoof designers to freeze the roll, which decreases one DOF of their design.

Previous research found that sliding between the foot and ground has to be controlled to avoid falling and slipping [34]. However, sliding is caused by the transverse force applied to the foot when it is in contact with the ground. The findings of this article show that the energy needed to slide the hoof changes with the compliance levels. This implies that the transverse force is dynamically changed due to the coupled dynamics of the joints of the hoof and their interaction with the environment. Therefore, new field robots such as ScarlETH [35] and Anymal [36] from ETH Zurich, Big Dog [37] from Boston Dynamics, and RSTAR [38] could utilize this artificial hoof for improving their slip resistance.

The two main implications from this article were: 1) it contributed toward the simplification of robotic hooves and 2) it highlighted possible anatomical features such as compliance of the joints of the biological hoof that affect its slip resistance. These can be the basis for the development of other biological studies of the hoof, where the effects of the compliance of the joints can be further explored.

For instance, from a biological point of view, neural-level reflexes play a major role when a noticeable slip occurs within a short time. This article does not address such combined active control and passive mechanical reactions. A slip speed of 0.01 m/s minimizes the possibility of involving such reflex activities. A future study could address how the passive dynamics of the hoof vary for a range of speeds. The robotic hoof can also be further simplified by locking the fetlock joint angle to $\theta = 5^\circ$. The effects of flexion/extension at this joint on the slip resistance can also be studied.

Furthermore, developing a fabrication mechanism to incorporate compliant joints in the manufacturing process of robotic hooves would be one interesting possibility. The analysis and development of a method for real-time control of the compliance of hoof joints using methods presented in [39]–[41] could also allow a robot to adapt to different terrain conditions (such as deformable or inclined terrains). In addition, the findings of this article pose a viable hypothesis that the dynamics of the hoof plays an important role in slip resistance in biological goats. This should be verified in behavioral experiments with goats.

## ACKNOWLEDGMENT

The authors would like to thank G. Constantinescu for providing the figure of the hoof in large ruminants to illustrate the bones in the goats' hoof. The authors would also like to thank Wiley for providing the figure of the muscles and tendons of the goat's hoof. The authors would also like to thank the National University of Loja. More specifically, the authors would also like to thank R. M. Abad G. for his assistance in the field trips and the videos of the Ecuadorian goats utilized in this research.

## REFERENCES

[1] R. Pfeifer, M. Lungarella, and F. Iida, "Self-organization, embodiment, and biologically inspired robotics," *Science*, vol. 318, no. 5853, pp. 1088–1093, 2007.

[2] S. Seok, A. Wang, M. Y. Chuah, D. Otten, J. Lang, and S. Kim, "Design principles for highly efficient quadrupeds and implementation on the MIT cheetah robot," in *Proc. IEEE Int. Conf. Robot. Autom.*, May 2013, pp. 3307–3312.

[3] U. Saranli, M. Buehler, and D. E. Koditschek, "RHex: A simple and highly mobile hexapod robot," *Int. J. Robot. Res.*, vol. 20, no. 7, pp. 616–631, 2001.

[4] S. Kim, A. T. Asbeck, M. R. Cutkosky, and W. R. Provancher, "SpinybotII: Climbing hard walls with compliant microspines," in *Proc. 12th Int. Conf. Adv. Robot.*, Jul. 2005, pp. 601–606.

[5] H. W. Park, S. Park, and S. Kim, "Variable-speed quadrupedal bounding using impulse planning: Untethered high-speed 3D running of MIT Cheetah 2," in *Proc. IEEE Int. Conf. Robot. Autom.*, May 2015, pp. 5163–5170.

[6] J. B. Jeans and D. Hong, "IMPASS: Intelligent mobility platform with active spoke system," in *Proc. IEEE Int. Conf. Robot. Autom.*, 2009, pp. 1605–1606.

[7] A. M. Carroll, D. V. Lee, and A. A. Biewener, "Differential muscle function between muscle synergists: long and lateral heads of the triceps in jumping and landing goats (Capra hircus)," *J. Appl. Physiol.*, vol. 105, no. 4, pp. 1262–1273, 2008.

[8] A. S. Arnold, D. V. Lee, and A. A. Biewener, "Modulation of joint moments and work in the goat hindlimb with locomotor speed and surface grade," *J. Exp. Biol.*, vol. 216, no. 12, pp. 2201–2212, 2013.

[9] D. V. Lee, M. P. McGuigan, E. H. Yoo, and A. A. Biewener, "Compliance, actuation, and work characteristics of the goat foreleg and hindleg during level, uphill, and downhill running," *J. Appl. Physiol.*, vol. 104, no. 1, pp. 130–141, 2008.

[10] G. B. Gillis, J. P. Flynn, P. McGuigan, and A. A. Biewener, "Patterns of strain and activation in the thigh muscles of goats across gaits during level locomotion," *J. Exp. Biol.*, vol. 208, no. 24, pp. 4599–4611, 2005.

[11] T. McGeer and L. H. Palmer, "Wobbling, toppling, and forces of contact," *Amer. J. Phys.*, vol. 57, no. 12, pp. 1089–1098, 1989.

[12] Q. Zhang, K. Xu, and X. Ding, "Investigation of feet functions of large ruminants with a decoupled model of equivalent mechanism," *Biol. Open*, vol. 6, no. 4, pp. 407–414, 2017.

[13] Q. Zhang, X. Ding, and K. Xu, "Terrain adaptability mechanism of large ruminants' feet on the kinematics view," *Appl. Bionics Biomech.*, vol. 2015, 2015, Art. no. 151686.

[14] S.-A. Abad, N. Sornkarn, and T. Nanayakkara, "The role of morphological computation of the goat hoof in slip reduction," in *Proc. IEEE/RSJ Int. Conf. Intell. Robots Syst.*, 2016, pp. 5599–5605.

[15] T. O. McCracken, R. A. Kainer, and T. L. Spurgeon, *Spurgeon's Color Atlas of Large Animal Anatomy: The Essentials*. Hoboken, NJ, USA: Wiley-Blackwell, 2008.

[16] G. Constantinescu, *Guide to Regional Ruminant Anatomy Based on the Dissection of the Goat*. Hoboken, NJ, USA: Wiley, 2001.

[17] P. Khatun, C. M. Bingham, N. Schofield, and P. H. Mellor, "An experimental laboratory bench setup to study electric vehicle antilock braking/traction systems and their control," in *Proc. IEEE 56th Veh. Technol. Conf.*, Sep. 2002, vol. 3, pp. 1490–1494.

[18] T. Bera, K. Bhattacharya, and A. Samantaray, "Evaluation of antilock braking system with an integrated model of full vehicle system dynamics," *Simul. Model. Practice Theory*, vol. 19, no. 10, pp. 2131–2150, 2011.

[19] P. E. Wellstead and N. B. O. L. Pettit, "Analysis and redesign of an antilock brake system controller," *Proc. Inst. Elect. Eng.—Control Theory Appl.*, vol. 144, no. 5, pp. 413–426, Sep. 1997.

[20] M. H. Raibert, *Miembros Locomotores del Cerdo, in Anatomia Veterinaria*, 3rd ed. Mexico City, Mexico: Elsevier, 2007.

[21] J. Nourinezhad, Y. Mazaheri, and M. K. Mahabady, "Gross anatomy of the ligaments of fetlock joint in dromedary camel," *J. Camel Practice Res.*, vol. 18, no. 2, pp. 197–202, 2011.

[22] D. P. Manning, J. E. Cooper, C. Jones, and M. Bruce, "Slip-shod or safely shod: The bighorn sheep as a natural model for research." *J. Roy. Soc. Med.*, vol. 83, no. 11, pp. 686–689, Nov. 1990.

[23] K. Budras *et al.*, *Bovine Anatomy: An Illustrated Text* (Manson Series). Hannover, Germany: Schluetersche, 2003.

[24] R. Frandson, W. Wilke, and A. Fails, *Anatomy and Physiology of Farm Animals*. Hoboken, NJ, USA: Wiley, 2009.

[25] D. H. Chadwick, *A Beast the Color of Winter: The Mountain Goat Observed*. Lincoln, NE, USA: Univ. Nebraska Press, 2002.

[26] K. Johanastrom and C. Canudas-De-Wit, "Revisiting the LuGre friction model," *IEEE Control Syst.*, vol. 28, no. 6, pp. 101–114, Dec. 2008.

[27] C. C. De Wit, P. Tsiotras, E. Velenis, M. Basset, and G. Gissinger, "Dynamic tire friction models for vehicle traction/braking control," *Veh. Syst. Dyn.*, vol. 39, no. 3, pp. 189–226, 2003.

[28] E. Berger, "Friction modeling for dynamic system simulation," *Appl. Mech. Rev.*, vol. 55, no. 6, pp. 535–577, 2002.

[29] C. C. De Wit, H. Olsson, K. J. Astrom, and P. Lischinsky, "A new model for control of systems with friction," *IEEE Trans. Autom. Control*, vol. 40, no. 3, pp. 419–425, Mar. 1995.

[30] J. E. Vargas Bayona, L. Zaragoza Martínez, J. V. Delgado, and B. G. Rodríguez Galván, *Biodiversidad Caprina Iberoamericana*. Bogotá, Colombia: Ediciones Univ. Coopertiva de Colombia, 2017.

[31] A. M. F. González, "Caracterización fenotípica de la cabra criolla y su sistema de producción, en la parroquia limones del cantón zapotillo," B.S. thesis, Facultad Agropecuaria y de Recursos Naturales Renovables, Repositorio Univ. Nacional de Loja, Loja, Ecuador, Apr. 2018.

[32] *Ensemble MP Hardware Manual*, 4th ed., Aerotech, Pittsburgh, PA, USA, 2015.

[33] *U Channel Linear Motors Hardware Manual*, 2nd ed., Aerotech, Pittsburgh, PA, USA, 2012.

[34] J. D. Karssen, M. Haberland, M. Wisse, and S. Kim, "The effects of swing-leg retraction on running performance: Analysis, simulation, and experiment," *Robotica*, vol. 33, no. 10, pp. 2137–2155, 2015.

[35] M. Hutter, C. D. Remy, M. A. Hoepflinger, and R. Siegwart, "ScarlETH: Design and control of a planar running robot," in *Proc. IEEE/RSJ Int. Conf. Intell. Robots Syst.*, 2011, pp. 562–567.

[36] M. Hutter *et al.*, "ANYmal—A highly mobile and dynamic quadrupedal robot," in *Proc. IEEE/RSJ Int. Conf. Intell. Robots Syst.*, 2016, pp. 38–44.

[37] D. Wooden, M. Malchano, K. Blankespoor, A. Howardy, A. A. Rizzi, and M. Raibert, "Autonomous navigation for BigDog," in *Proc. IEEE Int. Conf. Robot. Autom.*, 2010, pp. 4736–4741.

[38] D. Zarrouk and L. Yehezkel, "Rising star: A highly reconfigurable sprawl tuned robot," *IEEE Robot. Autom. Lett.*, vol. 3, no. 3, pp. 1888–1895, Jul. 2018.

[39] L. Ding *et al.*, "Foot–terrain interaction mechanics for legged robots: Modeling and experimental validation," *Int. J. Robot. Res.*, vol. 32, no. 13, pp. 1585–1606, 2013.

[40] C.-L. Shih, J. W. Grizzle, and C. Chevallereau, "From stable walking to steering of a 3D bipedal robot with passive point feet," *Robotica*, vol. 30, no. 7, pp. 1119–1130, 2012.

[41] F. J. Comin and C. M. Saaj, "Models for slip estimation and soft terrain characterization with multilegged wheel–legs," *IEEE Trans. Robot.*, vol. 33, no. 6, pp. 1438–1452, Dec. 2017.

**Sara-Adela Abad** received the B.Eng. degree in electronic and control engineering from National Polytechnic School, Quito, Ecuador, in 2010, the M.Sc. degree in artificial intelligence from the University of Southampton, Southampton, U.K., in 2013, and the Ph.D. degree in robotics from the Dyson School of Design Engineering, Imperial College London, London, U.K., in 2019.

Her research interests include biologically inspired robots, soft robotics, and robots' adaptability to uncertain conditions.

**Nicolas Herzig** received the M.E. degree in mechanical engineering and the M.S. degree in mechatronics from Polytech Annecy Chambéry, Annecy, France, both in 2011, and the Ph.D. degree in control engineering from Institut National des Sciences Appliquées de Lyon, Université de Lyon, Lyon, France, in 2016.

He is currently a Research Associate with Imperial College London, London, U.K. His research interests include robotics, mechatronics, and control engineering for soft and compliant robotics.

**Seyedmohammadhadi M. Hadi Sadati** received the M.Sc. degree in mechanical engineering from the Sharif University of Technology, Tehran, Iran, in 2012, and the Ph.D. degree in robotics from King's College London, London, U.K., in 2017.

He is currently a Postdoctoral Research Associate in morphological computation with the University of Bristol, Bristol, U.K., working within the Leverhulme Trust Research Project "Computing with spiders' webs—An inspiration for new sensors and robots." He has been a Visiting Researcher with Imperial College London, London, U.K., and Clemson University, Clemson, SC, USA. His research interests include bioinspired soft robotics, morphological computation, stiffness controllable continuum manipulators, and dynamic systems.

**Thrishantha Nanayakkara** received the B.Sc. degree in electrical engineering from the University of Moratuwa, Moratuwa, Sri Lanka, in 1996, and the M.Sc. degree in electrical engineering and the Ph.D. degree in robotics from Saga University, Saga, Japan, in 1998 and 2001, respectively.

He was a Postdoctoral Research Fellow with the Department of Biomedical Engineering, Johns Hopkins University, Baltimore, MD, USA, from 2001 to 2003, a Senior Lecturer with the Faculty of Engineering, University of Moratuwa, a Radcliffe Fellow with Harvard University, Cambridge, MA, USA, from 2008 to 2009, a Research Affiliate with the Massachusetts Institute of Technology, Cambridge, MA, USA, from 2008 to 2009, and a Senior Lecturer with the Department of Informatics, King's College London, London, U.K., from 2009 to 2016. He is currently a Reader with the Dyson School of Design Engineering, Imperial College London, London. He has authored or coauthored one textbook and more than 150 peer-reviewed papers. His research interests include soft robotics and robotic interaction with uncertain environments.